



Alfvénic Perturbations in a Sunspot Chromosphere Linked to Fractionated Plasma in the Corona

Deborah Baker¹, Marco Stangalini², Gherardo Valori¹, David H. Brooks³, Andy S. H. To¹, Lidia van Driel-Gesztelyi^{1,4,5}, Pascal Démoulin⁴, David Stansby¹, David B. Jess^{6,7}, and Shahin Jafarzadeh^{8,9}

¹ University College London, Mullard Space Science Laboratory, Holmbury St. Mary, Dorking, Surrey, RH5 6NT, UK

² ASI Italian Space Agency, Via del Politecnico, s.n.c I-00133—Roma, Italia

³ College of Science, George Mason University, 4400 University Drive, Fairfax, VA 22030, USA

⁴ LESIA, Observatoire de Paris, Université PSL, CNRS, Sorbonne Université, Univ. Paris Diderot, Sorbonne Paris Cité, 5 place Jules Janssen, F-92195 Meudon, France

⁵ Konkoly Observatory, Research Centre for Astronomy and Earth Sciences, Hungarian Academy of Sciences, Konkoly Thege út 15-17., H-1121, Budapest, Hungary

⁶ Astrophysics Research Centre, School of Mathematics and Physics, Queen's University Belfast, Belfast, BT7 1NN, UK

⁷ Department of Physics and Astronomy, California State University Northridge, Northridge, CA 91330, USA

⁸ Rosseland Centre for Solar Physics, University of Oslo, P.O. Box 1029 Blindern, NO-0315 Oslo, Norway

⁹ Institute of Theoretical Astrophysics, University of Oslo, P.O. Box 1029 Blindern, NO-0315 Oslo, Norway

Received 2020 September 9; revised 2020 November 9; accepted 2020 November 15; published 2021 January 21

Abstract

In this study, we investigate the spatial distribution of highly varying plasma composition around one of the largest sunspots of solar cycle 24. Observations of the photosphere, chromosphere, and corona are brought together with magnetic field modeling of the sunspot in order to probe the conditions that regulate the degree of plasma fractionation within loop populations of differing connectivities. We find that, in the coronal magnetic field above the sunspot umbra, the plasma has photospheric composition. Coronal loops rooted in the penumbra contain fractionated plasma, with the highest levels observed in the loops that connect within the active region. Tracing field lines from regions of fractionated plasma in the corona to locations of Alfvénic fluctuations detected in the chromosphere shows that they are magnetically linked. These results indicate a connection between sunspot chromospheric activity and observable changes in coronal plasma composition.

Unified Astronomy Thesaurus concepts: Sunspots (1653); Magnetic fields (994); Solar active region magnetic fields (1975); Solar chromosphere (1479); Solar corona (1483)

Supporting material: animation

1. Introduction

Early observations of elemental abundance variations on the Sun showed systematic differences between the composition of the corona and that of the photosphere (e.g., Widing & Feldman 1989, 1995; Sheeley 1995, 1996). In the closed-loop solar corona, in the slow solar wind, and in solar energetic particles, elements with low first ionization potential (FIP < 10 eV) are more abundant by a factor of 2–4 compared to the photosphere (e.g., Meyer 1985a, 1985b; Gloeckler & Geiss 1989; Feldman & Widing 2003; Brooks et al. 2015), whereas high FIP elements (FIP > 10 eV) retain their photospheric elemental distribution. Plasma composition in the open magnetic field of coronal holes remains relatively unfractionated when it is observed in the corona (e.g., Feldman & Widing 1993; Doschek et al. 1998; Feldman et al. 1998; Brooks & Warren 2011). Abundance variations are typically characterized by FIP bias, which is the ratio of an element's abundance in the solar atmosphere to its abundance in the photosphere. FIP bias of ~ 1 indicates unfractionated photospheric plasma composition and > 1.5 is fractionated plasma of coronal composition.

Feldman et al. (1990) provided one of the few early studies of plasma composition around a sunspot based on spatially unresolved slit observations obtained from a rocket flight of the High Resolution Telescope and Spectrograph (HRTS). These authors determined that, in the atmosphere above a sunspot, the elemental abundances had a photospheric distribution compared to the plasma of the nearby plage region, which was

highly enriched in low FIP elements. Similarly, Sheeley (1995) noted in a *Skylab* slitless spectrogram that plasma above a sunspot umbra was enriched in high FIP Ne VI, whereas in the adjacent penumbra, the plasma was enriched in low FIP Mg VI. Plasma rich in Ne VI occurred only in areas of flux emergence in two nearby active regions.

Subsequent studies of high FIP bias plasma in active regions refer to features such as Mg IX sprays (Sheeley 1996), spikes at the edges of active regions (Young & Mason 1997), fan loops (Warren et al. 2016), and upflow/outflow regions (e.g., Brooks & Warren 2011). Typically, the magnetic field associated with these features is the decaying or dispersed unipolar areas of a strong magnetic field at the peripheries of active regions. Strong plasma fractionation is observed at the footpoints of loops rooted in the unipolar regions, where FIP bias levels are 3–4 (Brooks & Warren 2011; Baker et al. 2013; Brooks et al. 2015). High FIP bias of ~ 3 is also observed in the cores of quiescent active regions (Del Zanna & Mason 2014).

According to the plasma fractionation model of Laming (2015), a compelling explanation for the separation of ions from neutrals is the ponderomotive force arising from the reflection or refraction of Alfvén waves in the chromosphere. The Alfvén waves act only on the ions while leaving neutral elements unaffected. Though the fractionation is influenced by the origin and flux of the Alfvén waves as well as the wave–wave interactions in the chromosphere, in general, the time-averaged ponderomotive force is directed upward, giving rise to the enrichment of easy-to-ionize low FIP elements in the corona (Laming 2015, 2017). The direction and ultimately the

resonance of the Alfvén waves are all-important to the degree of fractionation observed in the corona (Laming et al. 2019). These features are set by where the Alfvén waves are generated. In open field regions, typical waves with 3 and 5 minute periods (e.g., Khomenko & Collados 2015, and references therein) generated from below the photosphere propagate upward at the base of the field and either continue along the open field or are reflected back down; there is little resonance and therefore little fractionation. Upward-propagating waves with such long periods do not resonate with the closed-loop corona, so as with open field regions, the waves are reflected back down at the loop footpoints, resulting in little or no fractionation. Conversely, Alfvén waves generated in the corona due to magnetic reconnection are directed downward to loop footpoints at the top of the chromosphere and then are reflected back upward at the steep density gradient located there. Laming (2017) proposed that resonant waves are excited within the coronal loop itself as a result of nanoflare reconnection in the corona, thereby creating enhanced fractionation at magnetically connected loop footpoints (Baker et al. 2013; Dahlburg et al. 2016; Laming 2017; Laming et al. 2019). It is not observationally clear, however, whether these oscillations generated by reconnection in the corona are linked to enhanced fractionation.

In this regard, the quest for magnetic fluctuations associated with magnetohydrodynamic waves (MHD) in solar magnetic structures assumes a particular importance. Observationally, MHD waves in solar magnetic structures are generally detected as intensity and velocity oscillations (Bogdan 2000; Centeno et al. 2006; Chorley et al. 2010; Morton et al. 2011; Stangalini et al. 2012; Grant et al. 2015; Jafarzadeh et al. 2017; Jess et al. 2017), although simultaneous magnetic fluctuations are also expected from theory for different types of MHD modes (Edwin & Roberts 1983; Roberts 1983). The required magnetic oscillations for ponderomotive fractionation to take place can therefore be associated with a number of different wave modes (Roberts 1983; Khomenko et al. 2003; Goossens et al. 2009; Morton et al. 2015), e.g., locally excited waves (Alfvén, magnetoacoustic fast mode in high- β regimes), or global eigenmodes of the magnetic structure (e.g., sausage mode, torsional Alfvén mode,...). We will refer to magnetic fluctuations associated with any wave mode as Alfvénic waves, to distinguish from a purely Alfvén mode. The detection of magnetic oscillations associated with MHD modes is a difficult task, as opacity effects or instrumental crosstalk with other physical quantities can easily mimic the effect of these oscillations (e.g., Khomenko & Collados 2015; Joshi & de la Cruz Rodríguez 2018, and references therein). One way to disentangle intrinsic magnetic oscillations in the solar atmosphere is through the investigation of the phase lag between the polarization signals associated with magnetic field disturbances and other physical quantities such as intensity and Doppler velocity (Stangalini et al. 2018, 2021). Oscillating physical quantities associated with MHD waves may have different phase relations depending on the MHD mode and the propagation state of the wave (Fujimura & Tsuneta 2009; Moreels et al. 2013; Moreels & Van Doorsselaere 2013; Hinode Review Team et al. 2019), thus the analysis of the phase relations between them can be exploited for their identification (Stangalini et al. 2018) as well as the identification of the specific mode producing them.

In this paper, we show a detailed, spatially resolved coronal composition map of a strong and coherent leading sunspot in AR 12546. We find that the elemental abundance variation in the corona above the sunspot is highly structured, with extremes in the level of fractionation among the distinct loop populations. The distribution of the highly fractionated plasma appears to be correlated with the spatial locations at which intrinsic magnetic oscillations are identified in nearly simultaneous high spatial resolution spectropolarimetric observations of the solar chromosphere (Stangalini et al. 2021). Magnetic field modeling is used to investigate the connectivities of the loop populations within the sunspot in order to seek an understanding of the distribution of plasma composition observed there. We interpret our findings in the wider context of coronal heating and the ponderomotive force model of elemental fractionation (Laming 2015).

2. Observations and Methods

2.1. Overview of AR 12546

The observations of AR 12546 were obtained on 2016 May 20 using the Hinode EUV Imaging Spectrometer (EIS; Culhane et al. 2007), the Interferometric BIdimensional Spectrometer at the National Solar Observatory Dunn Solar Telescope (IBIS; Cavallini 2006; Reardon & Cavallini 2008), the Solar Dynamics Observatory (SDO)/Atmospheric Imaging Assembly (AIA; Lemen et al. 2012), and the SDO/Helioseismic and Magnetic Imager (HMI; Scherrer et al. 2012). Figure 1 shows high-resolution (Morgan & Druckmüller 2014) SDO/AIA 193 Å (a) and 171 Å (b) context images centered on the active region, overlaid with contours indicating the positions of the EIS and IBIS fields of view (FOVs). At the time of the EIS raster, the sunspot is located at the solar central meridian (CM), approximately 100'' south of the equator. The bottom panel of the figure contains a series of SDO/HMI magnetograms (c–e), also with the EIS and IBIS FOVs overlaid. Figure 1 includes an animation of these observations for 2016 May 18–20.

AR 12546, one of the largest ARs of the last 20 years, was a relatively simple, bipolar region composed of a strong, coherent leading positive-polarity sunspot and a dispersed following field of negative polarity. Asymmetric flux concentrations are typical of bipolar regions; however, both the extent of the dispersion of the following polarity and the coherency of the leading spot are extreme in this case. At the time of its CM crossing on May 20, half of the total unsigned magnetic flux of the active region was 4.1×10^{22} Mx and the magnetic field strength was exceptionally high, exceeding 4000 G in the center of the sunspot umbra in the photosphere (Stangalini et al. 2018). There was no significant evolution of the large-scale field during the two days prior to the EIS and IBIS observations; the sunspot was globally stable. Small-scale evolution was limited to moving magnetic features streaming radially from the positive-polarity sunspot and ongoing fragmentation and dispersal of the negative field of the following polarity in the decaying active region (see also Murabito et al. 2019).

During the period of May 18–20, there were no flares > B-class nor coronal mass ejections attributable to AR 12546. The stability of the loops rooted in the sunspot umbra and penumbra and the lack of activity reflect the absence of consequential evolution in the magnetic field (see the included animation of Figure 1).

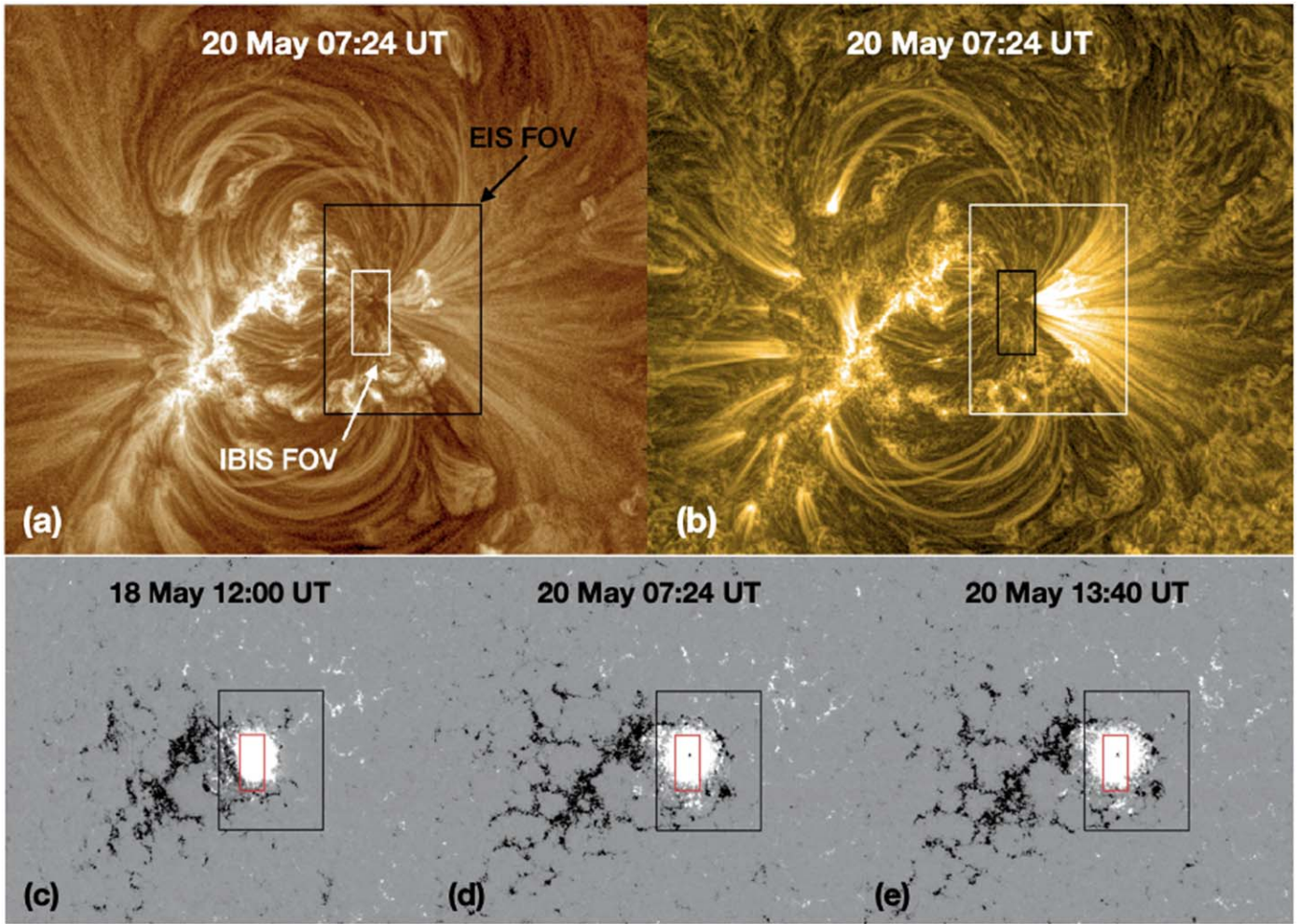


Figure 1. SDO/AIA 193 Å (a) and 171 Å (b) images at the time of the EIS observation at 07:24 UT on 2016 May 20. SDO/HMI magnetograms on May 18 at 12:00 UT (c), May 20 at 07:24 UT (d), and May 20 at 13:40 UT (e). All images are overlaid with boxes showing the larger Hinode/EIS (black) and smaller IBIS (red) FOVs. At 07:24 UT, the SDO/AIA and HMI FOV is $x = [-300'', 200'']$ and $y = [-280'', 140'']$. An animation of the figure is available. It covers the time period from 12:00 UT on May 18 to 14:55 UT on May 20 and has a real time duration of 30 s.

(An animation of this figure is available.)

2.2. IBIS Observations and Methods

IBIS full Stokes spectropolarimetric scans were used to identify possible signatures of magnetic field oscillations in circular polarization (CP) measurements in the umbra. A full account of the observations and data reduction techniques is provided in Stangalini et al. (2018), Murabito et al. (2020), Houston et al. (2020), and Stangalini et al. (2021). Here, we precis the aspects that are relevant to this analysis. The data set consists of a time series of Ca II 8542 Å scans beginning at 13:39 UT on May 20 and continuing for 184 minutes at a cadence of 48 sec. The Ca II is a chromospheric magnetically sensitive line and therefore suitable for detecting magnetic field oscillations at chromospheric heights. Figure 2 shows an IBIS intensity image in the photospheric Fe I 6173 Å line (a), for context, as well as an intensity image in the Ca II 8542 Å line (b). The IBIS FOV of $28'' \times 70''$ encompasses the umbra in the x -direction and a significant portion of the penumbra in the y -direction. The CP measurements were obtained from the amplitude of the Stokes-V profile. CP is defined as follows:

$$CP = \frac{|V_{\max}|}{I_{\text{cont}}} \cdot \text{sign}(V_{\max}), \quad (1)$$

where V_{\max} is the maximum amplitude of the Stokes V spectral profile and I_{cont} is the local continuum intensity (Stangalini et al. 2018).

To identify possible intrinsic magnetic field oscillations in the same IBIS data set, Stangalini et al. (2021) performed a specific phase lag analysis between the CP and the core intensity of the Ca II. Figure 2(c) shows the Stokes V_{\max}/I_{cont} CP map saturated at 0.3. The authors selected the CP instead of Doppler velocity of the Ca II line for the phase lag analysis, due to the presence of shocks that can turn the Ca II line from absorption to emission, rendering the line Doppler velocity undefined. The CP is directly related to line-of-sight magnetic field, but its variation can be caused by either intrinsic magnetic oscillations or opacity effects. In the case of opacity effects, the intensity is expected to be in/out of phase due to the fluctuation of the line formation height. This does not mean that real magnetic waves with the same phase relations (i.e., $\pm \pi$) do not exist, but the phase lag analysis provides a high level of confidence that we are not observing a mix of real and unreal oscillations. A strong coherence is needed to ensure that unreliable phase measurements are excluded from the analysis. In this work, we make use of the results of Stangalini et al.

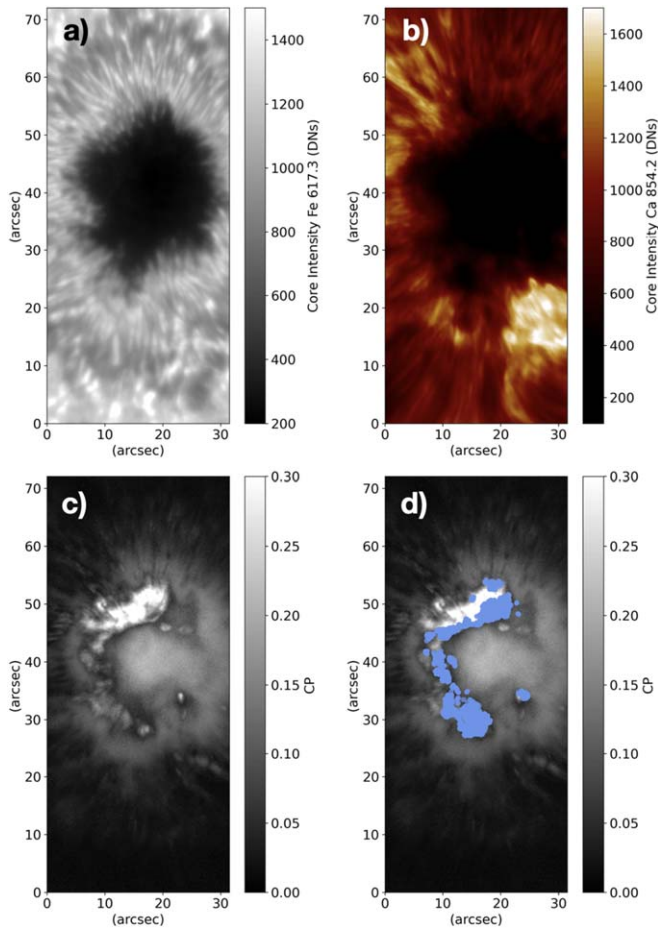


Figure 2. Top: photospheric IBIS Fe I 6173 Å (a) and chromospheric Ca II 8542 Å core intensity (b) images at 13:39 UT on 20 May. Bottom: Stokes V_{\max}/I_{cont} CP map without/with (c/d) blue dots overplotted. Blue dots indicate the locations where the magnetic waves are detected (see Figures 5, 6, as well as the discussion in Section 4). CP map is saturated at 0.3 (white).

(2021) and investigate the spatial distribution of the CP oscillations with the aim of assessing their role in the distribution of the observed FIP bias in and around the sunspot.

2.3. Hinode/EIS Observations and Methods

Hinode/EIS spectral data were used for the plasma composition analysis of the sunspot within AR 12546. An FOV of $120'' \times 160''$ was created using the $2''$ slit in $2''$ steps, taking 60 sec exposures at each slit position. The single scan began at 07:24 UT on May 20 and finished two hours later. Study #404 (Atlas _ 60) is a full spectral atlas of both CCDs, therefore it contains the diagnostic spectral lines required for constructing a spatially resolved composition map.

Data reduction was carried out using the `eis_prep` routine that is available in Solar SoftWare (Freeland & Handy 1998). The CCD signal in each pixel was converted into calibrated intensity units of $\text{erg cm}^{-2} \text{s}^{-1} \text{sr}^{-1} \text{\AA}^{-1}$, and pixels affected by cosmic ray hits, dust, and electric charge were removed/replaced. All data were corrected for instrumental effects of orbital spectrum drift (Kamio et al. 2010), CCD spatial offsets, and the grating tilt.

To construct the composition map, spectral lines from consecutive ionization stages of Fe VIII–Fe XVII and the low FIP Si X (FIP = 8.15 eV) and high FIP S X (FIP = 10.36 eV)

Table 1
Hinode/EIS Emission Lines

Diagnostics	Ion	Wavelength (Å)
Emission Measure	Fe VIII	185.21, 186.60
	Fe IX	188.50, 197.86
	Fe X	184.54
	Fe XI	188.21(b)
	Fe XII	192.39, 195.12(b)
	Fe XIII	202.04, 203.83(b)
	Fe XIV	264.79, 270.52(b)
	Fe XV	284.16
	Fe XVI	262.98
	Fe XVII	254.87
FIP Bias	Si X	258.38
	S X	264.23
Density	Fe XIII	202.04, 203.83(b)

Note. Blended lines (b) are fit with multiple Gaussian functions.

were fit with single Gaussian functions—except where the lines are blended, in which case the lines were fit with multiple Gaussian functions. The Si X/S X line ratio was used to determine FIP bias, and the density was measured with the Fe XIII 202.04 Å / 203.83 Å line ratio. The specific emission lines are given in Table 1. The CHIANTI Atomic Database, Version 8.0 (Dere et al. 1997; Del Zanna et al. 2015) was used to carry out the contribution function calculations, applying the photospheric abundances of Grevesse et al. (2007) for all of the spectral lines while assuming the measured Fe XIII densities. The Markov Chain Monte Carlo (MCMC) algorithm contained within the PINTofALE software package (Kashyap & Drake 2000) was used to compute the emission measure (EM) distribution for the Fe lines. The EM distribution was then convolved with the contribution functions and fit to the observed intensities of the low FIP Fe spectral lines. Si is also a low FIP element, therefore the EM derived from the Fe lines was scaled to reproduce the intensity of the Si X line. Finally, the FIP bias was determined to be the ratio of the predicted to the observed intensity for the high FIP S X line. The estimated uncertainty of the FIP bias ratio is 0.30, assuming an intensity error of 20%. A full account of the method is available in Brooks et al. (2015) and Baker et al. (2018).

Fe XII 195.12 Å relative Doppler velocities were measured versus a reference wavelength defined by averaging the centroid wavelengths of all pixels within the data array. This method was adopted because EIS does not have an absolute wavelength calibration. Excess broadening in the deblended Fe XII 195.12 Å emission line spectra was calculated from

$$\delta\lambda = \frac{\lambda_0}{c} \sqrt{4 \ln 2 \left(\frac{2 k_B T_i}{m} + \xi^2 \right) + \sigma_I^2}, \quad (2)$$

where $\delta\lambda$ is the observed line width, λ_0 is the line centroid, k_B is Boltzmann’s constant, T_i is the ion temperature, m is the mass, ξ is the nonthermal velocity, and σ_I is the instrumental width (e.g., Brooks & Warren 2016). Figure 3 shows the Hinode/EIS Fe XII intensity, Doppler and nonthermal velocity maps, Si X/S X composition map, and Fe XIII density map at 07:24 UT on 2016 May 20. SDO/HMI continuum contours have been overplotted on the EIS maps to mark the umbral and penumbral boundaries of the sunspot.

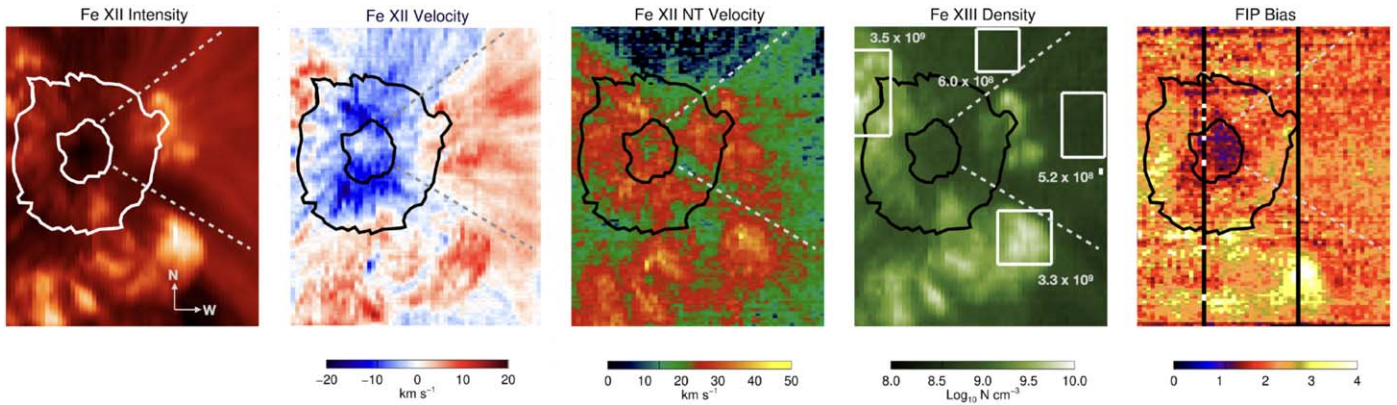


Figure 3. Hinode/EIS Fe XII intensity, Doppler velocity, nonthermal velocity maps, Fe XIII density, and Si X/S X FIP bias (or composition) maps at 07:24 UT on 20 May 2016. SDO/HMI continuum contours show the locations of the umbra and penumbra boundary. Dashed lines enclose the fan loops rooted on the western side of the sunspot. EIS FOV is $x = [-60'', 60'']$ and $y = [-170'', -30'']$ (coordinates from Sun center). Regions in the density map sample loop populations with mean density values provided for each white box. (Black stripes in the composition map are artifacts of the CCD and should not be confused with the IBIS FOV boundaries shown in the left panel of Figure 5).

Above the umbra, the plasma is blueshifted with upflow speeds of $10\text{--}20\text{ km s}^{-1}$ and nonthermal velocities ranging from $\sim 15\text{ km s}^{-1}$ above the center to $\sim 30\text{ km s}^{-1}$ toward the umbra/penumbra boundary. The plasma density is $\sim 5 \times 10^8\text{ cm}^{-3}$. The plasma composition above the umbra is photospheric, with a FIP bias of 1 above its core; toward the boundary, the composition becomes more fractionated, with FIP bias $\sim 1.5\text{--}2$, especially on the eastern edge.

Plasma parameters are more extreme above the penumbra, where the loops surrounding the sunspot are rooted. Upflows transition to downflows in the loops at the outer boundary. Nonthermal velocities are $30\text{--}50\text{ km s}^{-1}$ in loops located to the east and south of the penumbra; they are $\sim 30\text{--}40\text{ km s}^{-1}$ in the west (in between the dashed lines in the EIS maps). Plasma density increases by an order of magnitude above the penumbra compared with the umbra. FIP bias exceeds 3^+ above the eastern penumbra and reaches 4^+ at the boundary in the east and to the south. The strongest fractionation is located in the southern region in the vicinity of the highest nonthermal velocities of $45\text{--}50\text{ km s}^{-1}$.

3. Coronal Loop Connectivities

A Potential Field Source Surface (PFSS) extrapolation was computed to model the coronal loop system surrounding the sunspot. The rationale behind the use of the PFSS extrapolation is that this model captures the global field of the sunspot for comparison with the SDO/AIA coronal images of Figure 1. The PFSSPY package (Yeates 2018; Stansby 2020) was employed to extrapolate the coronal field from the HMI synoptic radial field map of CR2177. Figure 4 shows the extrapolation with selected field lines. A green contour represents 500 G in the positive-polarity sunspot. In general, there is good qualitative correspondence of the loops in the SDO/AIA images at the times of the EIS and IBIS observations with field lines in the extrapolation (Figure 4).

The coronal loop configuration of AR 12546 is characteristic of a bipolar region with distinct loop populations. Yellow field lines on the western side of the sunspot are long, extended loops that reach the source surface of the PFSS model ($=2.5 R_{\text{Sun}}$), therefore these field lines are considered to be open. To the north, the long, orange loops are connected with the negative polarity of the active region located to the northeast of

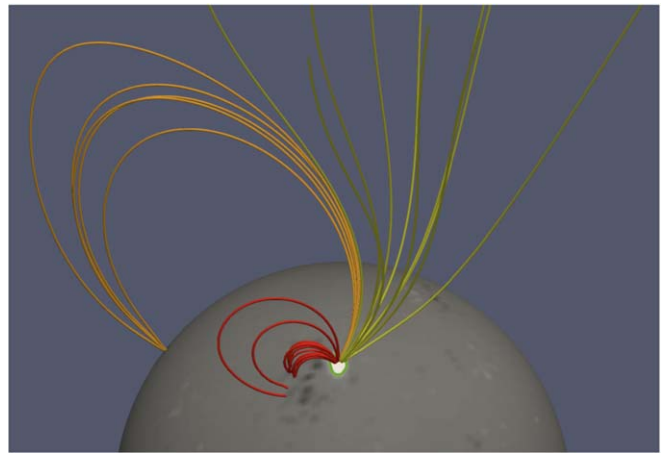


Figure 4. Selected field lines of the PFSS extrapolation of AR 12546 based on an SDO/HMI synoptic radial field magnetogram at 13:00 UT on 2016 May 20. Field lines are color-coded as closed within the same active region (red), closed to a neighboring active region (orange), or open (yellow); the radial magnetic field saturated at 100 G is represented in gray scale, and the green contour on the sunspot represents its 500 G isocontour.

AR 12546. The plasma density in these regions is $\sim 5\text{--}6 \times 10^8\text{ cm}^{-3}$ (see the mean densities within the boxes of the density map in Figure 3), and the plasma composition is partially fractionated, with FIP bias of 1.5–2. In contrast, the red loops on the east and south of the sunspot are compact loops that connect mainly with the opposite polarity within the active region. The density of the short, closed loops is an order of magnitude higher, and the plasma is highly fractionated, with FIP bias of 3–4.

4. Alfvénic Perturbations in the sunspot Chromosphere

Stangalini et al. (2021) found the presence of Alfvénic perturbations in the sunspot chromosphere in the 3 minute band of the IBIS Ca II time series (see Section 2.2). The frequency band corresponding to this period, which is also the dominant period in the solar chromosphere (e.g., Khomenko & Collados 2015, and references therein), is smaller than the ion-cyclotron frequency, and thus in the regime appropriate for the model of Laming (2015). A phase lag analysis between CP and intensity ruled out the possibility of opacity and other

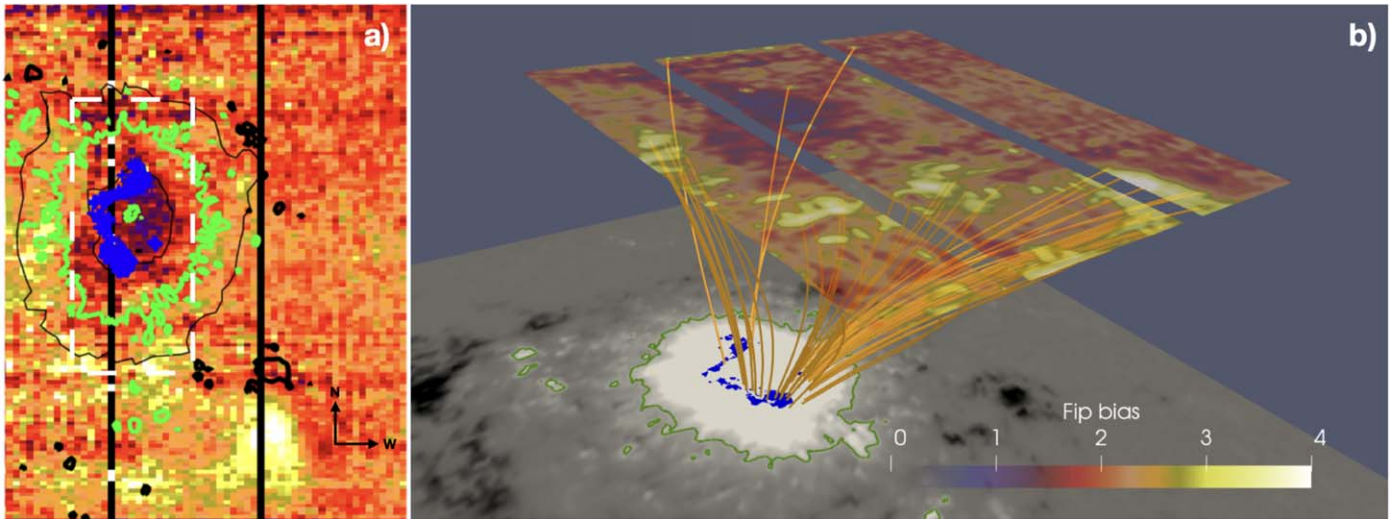


Figure 5. (a) Hinode/EIS Si X/S X FIP bias map at 07:24 UT on 2016 May 20. Contours: (i) SDO/HMI continuum umbra and penumbra boundaries (thin black lines), (ii) SDO/HMI LoS magnetogram ± 500 G (thick green/black lines = positive/negative polarity), (iii) location of Alfvénic waves from IBIS Ca II observation (blue dots), and (iv) IBIS FOV (white dashed box). (b) Selected high FIP bias field lines connecting high FIP bias in the corona to the umbra-penumbra boundary (orange), starting from values of FIP bias > 2.7 . Height of the FIP bias map is $z = 3.6$ CEA-deg and the value of the linear force-free parameter $\alpha = -0.2$ CEA-deg $^{-1}$. (Conversion factor is 1 CEA-deg $\simeq 12.17$ Mm.) Green contour represents the 500 G isocontour of the vertical magnetic field in the SHARP data.

spurious effects by identifying a specific phase lag of the order of -35 degrees between the two quantities, which is not consistent with the phase values expected from cross-talk or radiative opacity effects. Due to the vertical gradient of the magnetic field, any plasma density perturbation can induce a height variation of the response function of the spectral line, thus resulting in an observed spurious magnetic oscillation that is merely a consequence of an opacity change and has nothing to do with a real magnetic wave. In this regard, the study of the phase relation between different diagnostics is helpful in the identification of real magnetic oscillations. Indeed, by collecting phase measurements corresponding to high coherence, it was possible to discriminate between different effects and identify real magnetic oscillations in the sunspot chromosphere. Coherence is independent of the wave amplitude, thus this technique is able to detect correlations between two signals even if their amplitudes are small. It is worth noting that Alfvénic shocks were independently detected by Houston et al. (2020) at the same spatial locations, thereby confirming the interpretation of these disturbances in terms of real magnetic fluctuations. The locations of the Alfvénic perturbations are indicated by the blue dots overplotted on the Hinode/EIS FIP bias map of Figure 5(a) and on the CP map in Figure 2(d). The dots are aligned in a distinct C-shaped structure running from the north to the south along the eastern edge of the sunspot umbra.

Within the same EIS FOV in Figure 5(a), coronal loops containing highly fractionated plasma are present with particularly high values both to the east and to the southwest of the sunspot. The projected spatial proximity of the C-shaped structure and high FIP bias values poses the question of whether the loops of highly fractionated plasma observed in the corona are magnetically connected to the specific locations of Alfvénic perturbations in the chromosphere identified by Stangalini et al. (2021). The context for this question is provided by theoretical models based on the hypothesis that the fractionation process producing the FIP effect is powered by the conversion of magnetic waves at chromospheric heights (e.g., Schwadron et al. 1999; Laming 2015).

In order to answer this question, we need a magnetic model of the sunspot area—one that is representative of the sunspot field, so that we can determine whether the field lines threading regions of high FIP bias values are rooted in the blue dots of Figure 5. The main difficulty is that the FIP bias map is the result of a pixel-dependent, line-integrated emission of coronal lines to which it is challenging to attribute a height, and even more so a single height for the entire map. In addition, the paths followed by the modeled field lines depend on the properties of the chosen magnetic field model. Finally, there are more than eight hours between the beginning of the EIS observation, which was used to compute the FIP bias map, and the end of the IBIS observation, which was used to identify the Alfvénic perturbations. This complicates the alignment of the different observations, especially considering that both EIS and IBIS lack absolute pointing information. Therefore, the choice of the time of the magnetic field observations that are used to build the magnetic field model is also a factor of uncertainty. Given these difficulties, we adopted a heuristic approach by testing whether a combination of magnetic model and height of the FIP bias map exists where field lines starting from areas of high FIP bias values are rooted in the proximity of the blue dots.

A magnetic model for the sunspot can be obtained using a force-free extrapolation of photospheric measurements (see, e.g., Wiegmann & Sakurai 2012). The photospheric magnetogram used as input for the extrapolation is the SDO/HMI SHARP magnetogram taken at 13:00 UT, in between the end of EIS rastering and the start of the IBIS observation. SHARP data provide vector magnetograms of regions of the Sun in a Cylindrical Equal Area (CEA) projection, where the spatial dimensions are given in CEA degrees with 0.03 CEA-deg $\simeq 0''.5 \simeq 365$ km at the center of the disk. We use this approximate conversion factor in the scale estimations given below. The full SHARP field presents a significant flux imbalance (about 15%), therefore we use the linear force-free extrapolation method of Seehafer (1978), which does not require strict flux balance to be enforced. The entire FOV of the SHARP magnetogram covering an area of 22.89×12.99 CEA-deg was used to compute the Fourier coefficient of

Seehafer’s solution. However, in order to reduce the computing time required by the parametric study described below, the extrapolated magnetic field was computed in a smaller volume above the sunspot of size [11.22, 11.22, 16] CEA-deg. The extrapolation volume was discretized with a uniform resolution of 0.06 CEA-deg in the horizontal directions and with an exponentially stretched axis in the vertical direction, such that the pixel size increases from 0.06 at the bottom to 0.96 at the top.

The ratio of the vertical current density to the vertical magnetic field, $\alpha_{NL} = J_z/B_z$, represents the local torsion of field lines and is constant along individual field lines in force-free extrapolations. Within the linear approximation, this function is a free, constant parameter that is limited in magnitude by the inverse of the linear dimension of the extrapolated magnetogram. For Seehafer’s method applied to the entire FOV of the SHARP magnetogram, $\alpha_{\max} = 0.27$ CEA-deg $^{-1}$ (corresponding to 0.022 Mm $^{-1}$). Different magnetic field models are then obtained for different values of the constant α ($|\alpha| < \alpha_{\max}$) and the same magnetogram at the bottom boundary.

The alignment problem between the magnetic model based on the reprojected SDO/SHARP magnetogram on the one hand and the plane-of-the-sky SDO/AIA, IBIS, and EIS observations on the other was treated as follows. First, the locations of the Alfvénic perturbations were derotated from 13:39 UT (starting time of the IBIS measurements) to the starting time of the EIS raster. Second, since both EIS and IBIS lack absolute pointing information, the EIS raster and derotated locations of Alfvénic perturbations were aligned to multiple images of SDO at the time of the EIS raster. In particular, this operation produces a coalignment between the (derotated) location of the Alfvénic perturbations and the HMI line-of-sight magnetogram at 07:24 UT. Finally, a 500 G isocontour of the latter was used to match a similar contour in the SHARP vertical magnetic field (at 13:00 UT) to coalign the location of the Alfvénic perturbations and FIP bias map with the extrapolated field of the coronal models.

In summary, the heuristic method that we adopted consists of the following steps:

1. Producing magnetic field models for different (constant) α values between $-\alpha_{\max}$ and $+\alpha_{\max}$.
2. For each field model, placing the coaligned FIP bias map at different heights.
3. For each height of the FIP bias map, tracing the field lines in the given model starting from FIP bias values above 2.7 in the entire EIS FOV. The value 2.7 is chosen as the lowest possible value consistent with capturing most of the yellow area in the Figure 5(a), but reducing the number of pixels at the edge of the FIP bias map. This is done to avoid having the rectangular shape of the EIS FOV produce a misleading boundary of the field line distribution in the following steps. The filtering of field line seeds results in selecting relatively high FIP bias field lines. As an example, Figure 5(b) shows the 3D rendering of the spatial arrangement of Alfvénic oscillations (blue dots), a few selected field lines (orange), and the EIS map for the parameters of Figure 6(g).
4. Flagging the footpoints of the field lines with high FIP bias at chromospheric heights (1’’).

5. Comparing the location of the footpoints of field lines with high FIP bias with the location of the coaligned Alfvénic oscillations.
6. Finally, verifying if combinations of α and FIP bias map height exist that produce a distribution of high FIP bias field line footpoints similar to the distribution of blue dots in Figure 5(a).

The above procedure yielded the maps in Figure 6(b)–(h), where in addition to the blue dots representing the location of Alfvénic oscillations, the footpoints of the high FIP bias field lines are shown as orange dots. These maps provide an answer to our initial question: there are indeed combinations of model parameters for which the orange and blue dots are closely located. In other words, our parametric, heuristic study supports the existence of a magnetic link between high FIP bias values and the locations of Alfvénic perturbations in the chromosphere identified by Stangalini et al. (2021).

One can further try to deduce which is the value of α that results in the best match between the orange and blue dots in Figure 6(b)–(h). This is inevitably very subjective, as it strongly depends on which subset of dots is given priority in the match. If, for instance, only the number of orange dots overlapping the blue structure is considered, one would likely choose the potential case ($\alpha = 0$ in panel e) or even a slightly positive value of α as the best-matching case. This criterion discards the more isolated dots in the center and upper parts of the sunspot as not being significant. On the other hand, if the shape of the distribution is chosen as the primary matching criteria, then one may recognize how, similarly to the blue dots, the orange dots in Figure 6(b)–(h) are arranged in a pattern roughly shaped as a C with straight arms (except for few orange dots in the center of the sunspot). The red arrows on panels (e) and (g) of Figure 6 indicate how the arms of the C shape of the orange dots in two cases are identified. For instance, as the annotations in panel (e) indicate, in the potential case, both the vertical and upper orange arms are at an angle with the corresponding blue arms, whereas we deem the overlap of the whole structures to be better in panel (g). By matching the blue and orange C shapes as a whole, we would then identify the $\alpha = -0.2$ CEA-deg $^{-1}$ as the best-matching case.

Hence, adopting different matching criteria results in different values for the best-matching α , pointing at the limitations that a constant- α model of the magnetic field has in this particular application. Also, we stress again that treating the FIP bias map as a flat horizontal plane at a given height is a very crude approximation. On the other hand, the range of heights between 40 and 55 Mm of the FIP bias maps identified in Figure 6(b)–(h) yields coronal electron temperatures in the range of $\approx[0.9, 1.2]$ MK, assuming hydrostatic equilibrium (Aschwanden & Schrijver 2002). This is consistent with the temperature range for which the Si X–S X FIP bias line pair is an effective diagnostic of coronal plasma composition (Feldman et al. 2009; Brooks & Warren 2011).

The space-dependent distribution of α in the sunspot area can be computed as J_z/B_z using the photospheric observation of the SHARP magnetogram. This is plotted in Figure 6(a), with the blue contour identifying the distribution of the blue dots, showing that, while still predominantly positive, α values of both signs are present. It is interesting to note that a C-shaped concentration of negative α values is present right to the east of the C-shaped contour of the blue dots. The blue

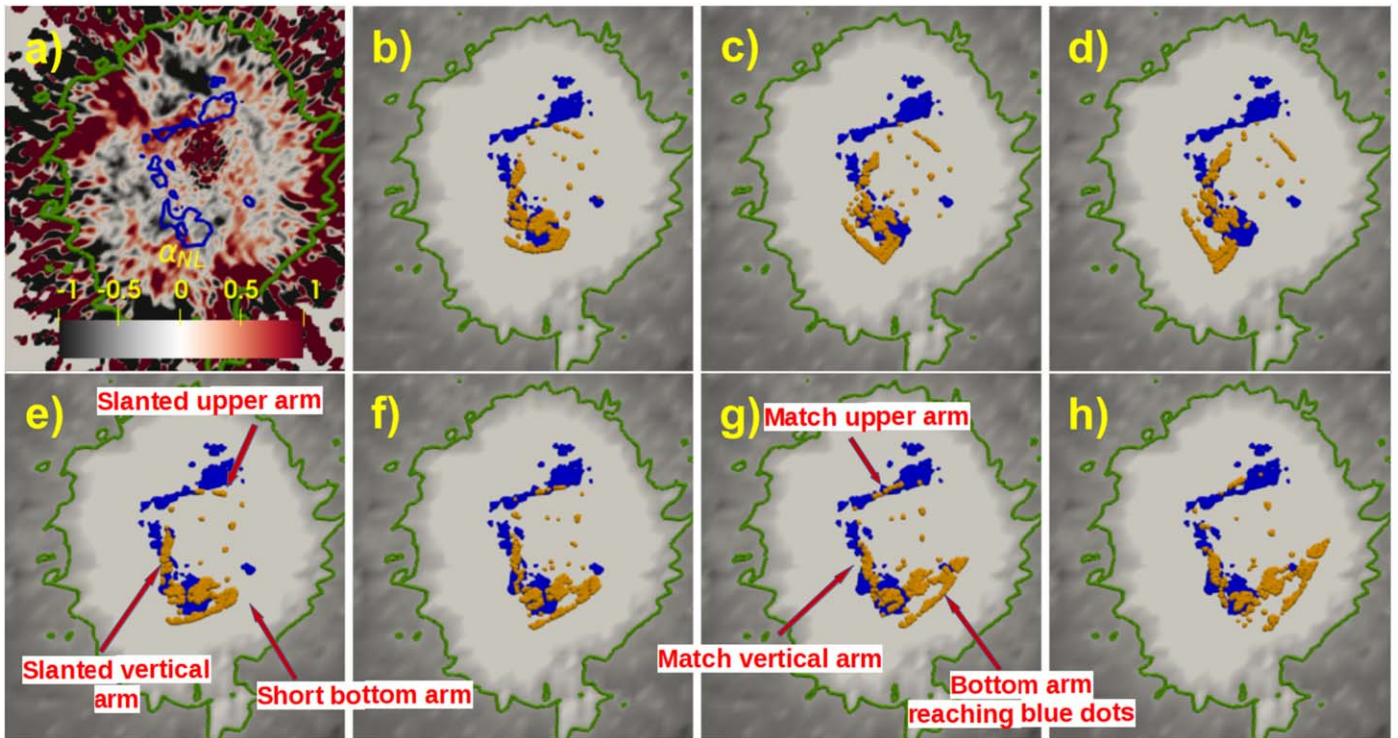


Figure 6. (a) Distribution of α_{NL} on the sunspot, saturated between -1 and 1 , derived from the SHARP magnetogram. Blue contour identifies the spatial distribution of the blue dots in panels (b–h). The remaining panels (b–h) illustrate the match between the footpoints of high FIP bias field lines (orange dots) and the location the Alfvénic perturbation (blue dots), for positive values of $\alpha = 0.1, 0.2, 0.25$ (panels b–d, respectively), for $\alpha = 0$ (panel e), and for negative values of $\alpha = -0.1, -0.2, -0.25$ (panels f–h, respectively), in CEA-deg $^{-1}$. The selected heights of the FIP bias maps are 3.6, 4.2, 4.5, 3.3, 3.3, 3.6, 3.6 CEA-degrees for cases (b–h), respectively. The conversion factor is 1 CEA-deg $\simeq 12.17$ Mm. In all panels, the green contour represents the 500 G isocontour of the vertical magnetic field in the SHARP data. Annotations on panels (e) and (g) highlight the matching criteria discussed in the text.

contour and the negative α values are not exactly overlapping, but their appearance is very similar in shape, with just a slight shift (of about 0.3 CEA-deg) that is comparable to the alignment accuracy among the different instruments/maps. The possible spatial correlation between Alfvénic oscillations and negative values of α suggested by Figure 6(a) is interesting because it may give some clues about the background field in which the oscillations took place. However, given the limitations of alignment and modeling discussed so far, we will not pursue this point any further; instead, we leave the investigation of this aspect to future studies on the nature of the Alfvénic oscillations (e.g., Section 6).

In summary, the heuristic method defined two parameters (the magnetic twist and the height of the FIP bias map) that resulted in a positive spatial correlation between high values of FIP bias and the Alfvénic 3 minute magnetic oscillations detected in the IBIS Ca II time series by Stangalini et al. (2021). This is indicative of a magnetic connection between chromospheric magnetic oscillation regions and high values of FIP bias observed in the corona above the sunspot. Given the intrinsic limitations of observations and magnetic modeling discussed above, these findings are nevertheless consistent with the theory of FIP fractionation outlined in Laming (2015).

5. Discussion

In this work, we have investigated the spatial distribution of coronal plasma composition in the vicinity of the large sunspot of AR 12546. Hinode/EIS observations revealed that compositional variation ranged from little or no fractionation in the corona above the core of the umbra to partially or highly

fractionated plasma in groups of coronal loops rooted in the surrounding penumbra.

Using a PFSS extrapolation of the large scale magnetic field of the positive-polarity sunspot, we identified distinct loop populations based on their connectivities: open field or long loops connected externally to the negative polarity of an active region ~ 570 Mm to the northeast, and short, dense loops internally connected to the negative polarity of the active region.

Plasma composition is relatively uniform within each loop population but varies across populations. FIP bias was 1.5–2 in the open field or long loops connecting externally to another active region, whereas it was 3–4 in the loops connecting to the opposite polarity within AR 12546 (Figure 3). Loops within a particular group are likely to share similar global properties and evolve together. In AR 12546, the very simple bipolar topology, coupled with there being little evolution of the large-scale magnetic field prior to the EIS and IBIS observations, suggests that there was limited mixing of plasma compositions via magnetic reconnection of different loop populations.

Among the global properties shared by coronal loops within the same population, loop length and resonance frequencies are at least theoretically related to the observed plasma fractionation distribution in and around the sunspot. The Laming ponderomotive force fractionation model predicts that resonant Alfvénic waves, generated by nanoflare reconnection in the corona, increase plasma fractionation in the vicinity of footpoints of resonant closed loops, whereas there is little resonance and fractionation along open field. In support of the

Laming model, numerical simulations of Dahlburg et al. (2016) showed that ponderomotive acceleration occurs at loop footpoints as a consequence of MHD waves generated by magnetic reconnection in the corona and that the FIP effect is a natural outcome of coronal heating. Significantly, the ponderomotive acceleration increases with increasing temperature and with decreasing length in closed coronal loops in the simulations. In the corona above the umbra of the large sunspot, the field had photospheric plasma composition. At photospheric and chromospheric heights, sunspot umbrae are regions of temperature minima such that elements are mainly neutral or singly ionized (e.g., Loukitcheva et al. 2014; Lodders 2019). As a consequence, local temperatures are not high enough to create a sufficient reservoir of ionized elements in the chromosphere, inhibiting plasma fractionation. Plasma transported from the chromosphere to the coronal field above the umbra is therefore likely to be unfractionated photospheric plasma.

On the western side of the sunspot, which is magnetically connected to another active region or has open field lines, FIP bias values were somewhat higher, between 1.5 and 2. The highest FIP bias of 3–4 was found on the eastern/southern sides of the spot in high-temperature active region core loops. These loops are rooted in the penumbra and are subject to convection-driven footpoint motions, leading to higher-frequency heating than in the loops rooted in the umbra (see Del Zanna & Mason 2018, and references therein).

Our results are consistent with the predictions of the Laming model and the output from the simulations of Dahlburg et al. (2016), in that high FIP bias plasma occurs in short, high-temperature loops where nanoflaring in the model generates high Alfvénic wave flux that is amplified by resonance. In the other sets of loops with different connectivities, e.g., open field lines, lower wave flux is expected because there is no repeated reflection of any potential Alfvénic waves created there, and consequently, these loops are likely to contain plasma with lower FIP bias. In fact, these findings do not exclude other theoretical models based on either wave interactions with chromospheric ions (e.g., the ion cyclotron wave heating model of Schwadron et al. (1999)) or on processes linked to coronal heating (e.g., heat conduction of the thermoelectric driving model of Antiochos (1994)).

In the wider context, we still fundamentally lack an understanding of what is happening in the chromosphere when we see activity in the corona, and a key goal generally is to elucidate the connection between activity in the low atmosphere and observable changes higher up. We have found that the internally connecting core loops with the highest FIP bias are rooted in areas where the Alfvénic perturbations were found in the chromosphere. This is the first observational evidence of detectable Alfvénic perturbations in the chromosphere being linked to coronal loops containing highly fractionated plasma. Whether this is the result of a response to coronal heating, as in the ponderomotive force model, or further evidence of heating at coronal heights being driven from below, remains an open question.

6. Concluding Remarks

This work represents a first attempt to investigate the role of magnetic fluctuations in plasma fractionation, made possible thanks to nearly simultaneous observations at chromospheric and coronal heights by IBIS and EIS, respectively. Our results

demonstrate a possible link between magnetic perturbations, observed at chromospheric heights as small fluctuations of the spectropolarimetric quantities, and the locations of high FIP bias observed in the corona. They therefore observationally support a role for MHD waves in the generation of the FIP effect and wave-based theoretical models.

Some questions still remain open, and thus identify possible future research directions. As already mentioned, magnetic fluctuations are expected for a number of different MHD wave modes. These can be magnetoacoustic modes that are locally excited within the umbra by residual convection and/or p-mode absorption, or globally excited eigenmodes of the sunspot. In this study, the exact identification of the wave mode responsible for the observed magnetic fluctuations was not possible with the available data. Indeed, different modes can coexist in the same structure, hampering the identification process. However, as noted in Stangalini et al. (2021), the locations where the Alfvénic waves are observed correspond to a narrow range of magnetic field inclinations, suggesting a possible role of the magnetic field geometry. In this regard, it is worth recalling that MHD waves in magnetic structure can undergo a mode conversion at the Alfvén-acoustic equipartition layer, with part of the energy contained in the acoustic-like components (fast MHD mode in the plasma- $\beta > 1$ regime) being converted to a combination of fast magnetoacoustic (in the plasma- $\beta < 1$ regime) and magnetic-like waves. This physical mechanism is dependent on the attack angle between the wavevector and the field lines (e.g., Gary 2001; Newington & Cally 2010; Cally 2011; Hansen et al. 2016), thus Stangalini et al. (2021) speculated on the possible role of the mode conversion and magnetic field geometry in the appearance of magnetic waves at chromospheric heights. In support of this scenario, Grant et al. (2018) uncovered evidence for Alfvénic waves, with the observed signatures being consistent with induced ponderomotive forces at the umbra/penumbra boundary of a sunspot chromosphere, suggesting that such wave-coupling effects may be linked to the increasing attack angles found in these locations.

Nevertheless, the Alfvénic waves identified by Stangalini et al. (2021) might be associated with different wave modes, not all of which necessarily produce the fractionation; however, they could be considered a proxy to identify the spatial locations where, given a magnetic field geometry, the conversion of acoustic-like to magnetic-like waves is particularly efficient.










In addition to the unambiguous identification of the wave process responsible for the magnetic waves, another important aspect is the propagation direction of the MHD waves, which plays a significant role in the FIP and I-FIP model of Laming (2015). Both the equipartition layer and the transition region can represent a reflective mirror for different types of waves (e.g., Hansen et al. 2016). For this reason, MHD waves can undergo several reflections/conversions, thus leaving open both the possibilities of waves coming from below or above (i.e., due to nanoflares).

In our view, these remain important aspects to be further addressed in the future, and they may provide useful information to constrain and validate existing theoretical models. The heuristic method employed in this study combines the linear extrapolation of photospheric magnetic field and the FIP bias map to investigate the possible connectivity of the Alfvénic chromospheric perturbations identified by Stangalini

et al. (2021). However, further studies that involve the full inversion of the chromospheric spectropolarimetric signals at the location of the perturbations are required in order to properly identify the properties of the background and transient magnetic field.

Hinode is a Japanese mission developed and launched by ISAS/JAXA, collaborating with NAOJ as a domestic partner and NASA and STFC (UK) as international partners. Scientific operation of Hinode is performed by the Hinode science team organized at ISAS/JAXA. This team mainly consists of scientists from institutes in the partner countries. Support for the post-launch operation is provided by JAXA and NAOJ (Japan), STFC (UK), NASA, ESA, and NSC (Norway). SDO data were obtained courtesy of NASA/SDO and the AIA and HMI science teams. D.B. and D.S. are funded under STFC consolidated grant number ST/S000240/1, and L.v.D.G. is partially funded under the same grant. L.v.D.G. acknowledges the Hungarian National Research, Development and Innovation Office grant OTKA K-131508. G.V. acknowledges the support from the European Union's Horizon 2020 research and innovation program under grant agreement No. 824135 and of the STFC grant No. ST/T000317/1. The work of D.H.B. was performed under contract to the Naval Research Laboratory and was funded by the NASA Hinode program. D.B.J. wishes to thank Invest NI and Radox Laboratories Ltd for the award of a Research & Development Grant (059RDEN-1). S.J. acknowledges support from the European Research Council under the European Unions Horizon 2020 research and innovation program (grant agreement No. 682462) and from the Research Council of Norway through its Centres of Excellence scheme (project No. 262622). The authors wish to acknowledge scientific discussions with the Waves in the Lower Solar Atmosphere (WaLSA; www.WaLSA.team) team, which is supported by the Research Council of Norway (project number 262622) and The Royal Society through the award of funding to host the Theo Murphy Discussion Meeting “High resolution wave dynamics in the lower solar atmosphere” (grant Hooke18b/SCTM). This research has received funding from the European Union's Horizon 2020 Research and Innovation program under grant agreement No 82135 (SOLARNET) and No 739500 (PRE-EST). This research has made use of the IBIS-A archive. We recognize the collaborative and open nature of knowledge creation and dissemination, under the control of the academic community as expressed by Camille Noûs at <http://www.cogitamus.fr/indexen.html>.

ORCID iDs

Deborah Baker  <https://orcid.org/0000-0002-0665-2355>
 Marco Stangalini  <https://orcid.org/0000-0002-5365-7546>
 Gherardo Valori  <https://orcid.org/0000-0001-7809-0067>
 David H. Brooks  <https://orcid.org/0000-0002-2189-9313>
 Andy S. H. To  <https://orcid.org/0000-0003-0774-9084>
 Lidia van Driel-Gesztelyi  <https://orcid.org/0000-0002-2943-5978>
 Pascal Démoulin  <https://orcid.org/0000-0001-8215-6532>
 David Stansby  <https://orcid.org/0000-0002-1365-1908>
 David B. Jess  <https://orcid.org/0000-0002-9155-8039>
 Shahin Jafarzadeh  <https://orcid.org/0000-0002-7711-5397>

References

- Antiochos, S. K. 1994, *AdSpR*, **14**, 139
 Aschwanden, M. J., & Schrijver, C. J. 2002, *ApJS*, **142**, 269
 Baker, D., Brooks, D. H., Démoulin, P., et al. 2013, *ApJ*, **778**, 69
 Baker, D., Brooks, D. H., van Driel-Gesztelyi, L., et al. 2018, *ApJ*, **856**, 71
 Bogdan, T. J. 2000, *SoPh*, **192**, 373
 Brooks, D. H., Ugarte-Urra, I., & Warren, H. P. 2015, *NatCo*, **6**, 5947
 Brooks, D. H., & Warren, H. P. 2011, *ApJL*, **727**, L13
 Brooks, D. H., & Warren, H. P. 2016, *ApJ*, **820**, 63
 Cally, P. S. 2011, in ASI Conf. Ser. 2, First Asia-Pacific Solar Physics Meeting, ed. A. R. Choudhuri & B. Banerjee (Bengaluru: ASI), 221
 Cavallini, F. 2006, *SoPh*, **236**, 415
 Centeno, R., Collados, M., & Trujillo Bueno, J. 2006, *ApJ*, **640**, 1153
 Chorley, N., Hnat, B., Nakariakov, V. M., Inglis, A. R., & Bakunina, I. A. 2010, *A&A*, **513**, A27
 Culhane, J. L., Harra, L. K., James, A. M., et al. 2007, *SoPh*, **243**, 19
 Dahlburg, R. B., Laming, J. M., Taylor, B. D., & Obenshain, K. 2016, *ApJ*, **831**, 160
 Del Zanna, G., Dere, K. P., Young, P. R., Landi, E., & Mason, H. E. 2015, *A&A*, **582**, A56
 Del Zanna, G., & Mason, H. E. 2014, *A&A*, **565**, A14
 Del Zanna, G., & Mason, H. E. 2018, *LRS*, **15**, 5
 Dere, K. P., Landi, E., Mason, H. E., Monsignori Fossi, B. C., & Young, P. R. 1997, *A&AS*, **125**, 149
 Doschek, G. A., Laming, J. M., Feldman, U., et al. 1998, *ApJ*, **504**, 573
 Edwin, P. M., & Roberts, B. 1983, *Sol. Phys.*, **88**, 179
 Feldman, U., Schühle, U., Widing, K. G., & Laming, J. M. 1998, *ApJ*, **505**, 999
 Feldman, U., Warren, H. P., Brown, C. M., & Doschek, G. A. 2009, *ApJ*, **695**, 36
 Feldman, U., & Widing, K. G. 1993, *ApJ*, **414**, 381
 Feldman, U., & Widing, K. G. 2003, *SSRv*, **107**, 665
 Feldman, U., Widing, K. G., & Lund, P. A. 1990, *ApJL*, **364**, L21
 Freeland, S. L., & Handy, B. N. 1998, *SoPh*, **182**, 497
 Fujimura, D., & Tsuneta, S. 2009, *ApJ*, **702**, 1443
 Gary, G. A. 2001, *SoPh*, **203**, 71
 Gloeckler, G., & Geiss, J. 1989, in AIP Conf. Ser. 183, Cosmic Abundances of Matter, ed. C. J. Waddington (Melville, NY: AIP), 49
 Goossens, M., Terradas, J., Andries, J., Arregui, I., & Ballester, J. L. 2009, *A&A*, **503**, 213
 Grant, S. D. T., Jess, D. B., Moreels, M. G., et al. 2015, *ApJ*, **806**, 132
 Grant, S. D. T., Jess, D. B., Zaqarashvili, T. V., et al. 2018, *NatPh*, **14**, 480
 Grevesse, N., Asplund, M., & Sauval, A. J. 2007, *SSRv*, **130**, 105
 Hansen, S. C., Cally, P. S., & Donae, A.-C. 2016, *MNRAS*, **456**, 1826
 Hinode Review Team, Al-Janabi, K., Antolin, P., et al. 2019, *PASJ*, **71**, R1
 Houston, S. J., Jess, D. B., Keppens, R., et al. 2020, *ApJ*, **892**, 49
 Jafarzadeh, S., Solanki, S. K., Gafêira, R., et al. 2017, *ApJS*, **229**, 9
 Jess, D. B., Van Doorselaere, T., Verth, G., et al. 2017, *ApJ*, **842**, 59
 Joshi, J., & de la Cruz Rodríguez, J. 2018, *A&A*, **619**, A63
 Kamio, S., Hara, H., Watanabe, T., Fredvik, T., & Hansteen, V. H. 2010, *SoPh*, **266**, 209
 Kashyap, V., & Drake, J. J. 2000, *BASI*, **28**, 475
 Khomenko, E., & Collados, M. 2015, *LRS*, **12**, 6
 Khomenko, E. V., Collados, M., & Bellot Rubio, L. R. 2003, *ApJ*, **588**, 606
 Laming, J. M. 2015, *LRS*, **12**, 2
 Laming, J. M. 2017, *ApJ*, **844**, 153
 Laming, J. M., Vourlidas, A., Korendyke, C., et al. 2019, *ApJ*, **879**, 124
 Lemen, J. R., Title, A. M., Akin, D. J., et al. 2012, *SoPh*, **275**, 17
 Lodders, K. 2019, arXiv:1912.00844
 Loukitcheva, M., Solanki, S. K., & White, S. M. 2014, *A&A*, **561**, A133
 Meyer, J. P. 1985a, *ApJS*, **57**, 151
 Meyer, J. P. 1985b, *ApJS*, **57**, 173
 Moreels, M. G., Goossens, M., & Van Doorselaere, T. 2013, *A&A*, **555**, A75
 Moreels, M. G., & Van Doorselaere, T. 2013, *A&A*, **551**, A137
 Morgan, H., & Druckmüller, M. 2014, *SoPh*, **289**, 2945
 Morton, R. J., Erdélyi, R., Jess, D. B., & Mathioudakis, M. 2011, *ApJL*, **729**, L18
 Morton, R. J., Tomczyk, S., & Pinto, R. 2015, *NatCo*, **6**, 7813
 Murabito, M., Ermolli, I., Giorgi, F., et al. 2019, *ApJ*, **873**, 126
 Murabito, M., Guglielmino, S. L., Ermolli, I., Stangalini, M., & Giorgi, F. 2020, *ApJ*, **890**, 96
 Newington, M. E., & Cally, P. S. 2010, *MNRAS*, **402**, 386
 Reardon, K. P., & Cavallini, F. 2008, *A&A*, **481**, 897
 Roberts, B. 1983, *SoPh*, **87**, 77
 Scherrer, P. H., Schou, J., Bush, R. I., et al. 2012, *SoPh*, **275**, 207

- Schwadron, N. A., Fisk, L. A., & Zurbuchen, T. H. 1999, [ApJ](#), **521**, 859
- Seehafer, N. 1978, [SoPh](#), **58**, 215
- Sheeley, N. R., Jr. 1995, [ApJ](#), **440**, 884
- Sheeley, N. R., Jr. 1996, [ApJ](#), **469**, 423
- Stangalini, M., Baker, D., Valori, G., et al. 2021, [RSPTA](#), **379**, 20200216
- Stangalini, M., Giannattasio, F., Del Moro, D., & Berrilli, F. 2012, [A&A](#), **539**, L4
- Stangalini, M., Jafarzadeh, S., Ermolli, I., et al. 2018, [ApJ](#), **869**, 110
- Stansby, D., Yeates, A., & Badman, S. 2020, [JOSS](#), **5**, 2732
- Warren, H. P., Brooks, D. H., Doschek, G. A., & Feldman, U. 2016, [ApJ](#), **824**, 56
- Widing, K. G., & Feldman, U. 1989, [ApJ](#), **344**, 1046
- Widing, K. G., & Feldman, U. 1995, [ApJ](#), **442**, 446
- Wiegmann, T., & Sakurai, T. 2012, [LRSP](#), **9**, 5
- Yeates, A. 2018, antyeates1983/pfss: First Release of pfss code, v1.0, Zenodo, doi:[10.5281/zenodo.1472183](#)
- Young, P. R., & Mason, H. E. 1997, [SoPh](#), **175**, 523